RSC Advances

PAPER

View Article Online
View Journal | View Issue

Check for updates

Cite this: *RSC Adv.*, 2023, **13**, 33187

Facile aqueous synthesis and comparative evaluation of TiO_2-semiconductor and TiO_2-metal nanohybrid photocatalysts in antibiotics degradation under visible light†

Yuping Zhang,‡[a] Shijie Ju,‡[a] Gregori Casals, [bc] Jie Tang,[a] Yichao Lin,[a] Xiaofang Li,[a] Lihua Liang,[a] Zhiyu Jia, *[d] Muling Zeng*[a] and Eudald Casals *[a]

Received 13th September 2023
Accepted 5th November 2023

DOI: 10.1039/d3ra06231g

rsc.li/rsc-advances

Advanced oxidation processes using TiO_2-based nanomaterials are sustainable technologies that hold great promise for the degradation of many types of pollutants including pharmaceutical residues. A wide variety of heterostructures coupling TiO_2 with visible-light active nanomaterials have been explored to shift its photocatalytic properties to harness sun irradiation but a systematic comparison between them is lacking in the current literature. Furthermore, the high number of proposed nanostructures with different size, morphology, and surface area, and the often complex synthesis processes hamper the transition of these materials into commercial and effective solutions for environmental remediation. Herein, we have designed a facile and cost-effective method to synthesize two heterostructured photocatalysts representative of two main families of novel structures proposed, hybrids of TiO_2 with metal (Au) and semiconductor (CeO_2) nanomaterials. The photocatalysts have been extensively characterized to ensure a good comparability in terms of co-catalyst doping characteristics, morphology and surface area. The photocatalytic degradation of ciprofloxacin and sulfamethoxazole as target pollutants, two antibiotics of high concern polluting water sources, has been evaluated and CeO_2/TiO_2 exhibited the highest activity, achieving complete antibiotic degradation at very low photocatalyst concentrations. Our study provides new insights into the development of inexpensive heterostructured photocatalysts and suggests that the non-stoichiometry and characteristic d and f electronic orbital configuration of CeO_2 have a significantly improved role in the enhancement of the photocatalytic reaction.

1. Introduction

Water sources are becoming increasingly scarce due to various factors such as climate change, industrialization, and human activity. Antibiotic abuse and misuse are among the activities particularly detrimental to marine and fluvial ecosystems, and contribute to the development of antibiotic resistance. To address this problem, advanced oxidation processes (AOPs) have been identified as a promising approach to remove water pollutants, including pharmaceutical residues.[1–4] One widely used AOP is photocatalytic degradation using titanium dioxide (TiO_2) because of its high photocatalytic activity, fast electron transfer ability to molecular oxygen, high stability within a wide pH range, non-toxicity, and low-cost.[5,6] In the catalytic reaction, when TiO_2 absorbs photons with energies higher or equal to its band gap energy, electrons are promoted from the valence band to the conduction band which generates electron–hole pairs that can oxidize water or hydroxide ions to produce hydroxyl radicals. These radicals act as powerful oxidizing agents.[7] However, the wide band gap of TiO_2 limits its ability to utilize solar light and the recombination of photo-generated electrons and holes decrease the quantum efficiency.[8] To overcome these limitations, doping TiO_2 with metal ions such as Cr, V, and Fe was proposed in the 90s, showing a red shift of the band-edge of the TiO_2, and this allowed for the catalytic decomposition of NO into N_2, O_2, and N_2O under visible light.[9]

With the advent of nanotechnology, the development of heterostructured photocatalysts that involve the coupling of TiO_2 nanoparticles (NPs) with noble metal NPs (*e.g.* Pt, Pd and Au)[10–15] or semiconductor NPs (*e.g.* ZnO, Cu_2O, SnO_2, ZrO_2, WO_3,

---

[a] School of Biotechnology and Health Sciences, Wuyi University, Jiangmen 529020, PR China. E-mail: mulingzeng@163.com; wyuchemecm@126.com

[b] Biochemistry and Molecular Genetics Department, Clinical and Provincial Hospital of Barcelona, Barcelona 08036, Spain

[c] IDIBAPS Research Center, Barcelona 08036, Spain

[d] Key Laboratory of Cluster Science, Ministry of Education of China, Beijing Key Laboratory of Photoelectronic/Electrophotonic Conversion Materials, School of Chemistry and Chemical Engineering, Beijing Institute of Technology, Beijing 100081, PR China. E-mail: jzy@bit.edu.cn

† Electronic supplementary information (ESI) available. See DOI: https://doi.org/10.1039/d3ra06231g

‡ Both authors contributed equally to this study.

and CeO_2)[16–21] in different configurations such as core-shells or nanohybrids is an active field of research. These materials are usually chosen for their co-catalyst properties, the plasmonic effect, in the case of metal NPs, which enhances the absorption of light towards the visible range of sunlight, and because they promote the separation of the photoexcited charge carriers (electrons and holes), thus reducing their recombination which prolong the charge separation time and increase redox capacity.[22–25] In a typical report of photocatalytic degradation of pollutants using such NPs, a photocatalyst nanomaterial is proposed and different parameters are explored. For instance, in the case of Au/TiO_2, one of the most widely studied due to the non-toxicity and localized surface plasmon resonance exhibited by AuNPs[12,26–28] it has been shown, among others, how the photocatalytic properties are affected by the interface between Au and TiO_2,[29] the size and shape of Au,[30,31] and the oxidation state of TiO_2.[32] In the case of coupling TiO_2NPs with other semiconductor NPs, TiO_2/CeO_2 hybrid nanostructures are attracting more attention recently due to the improved textural and structural properties of TiO_2.[33–36] Different types of CeO_2/TiO_2 with different morphologies and textural parameters have been proposed and compared, but a literature review revealed that the preparation conditions of TiO_2/CeO_2 have not been investigated in detail to achieve a nanostructure prepared in an industrially feasible way,[37] and this is still a common hindrance for many advanced nanostructures.[38]

Herein, two of the proposed nanostructured TiO_2-based photocatalysts have been prepared using simple bench-top chemistry, which are representative of the metal (Au/TiO_2) and semiconductor (CeO_2/TiO_2) NP coupling. Furthermore, the photocatalytic degradation using Au/TiO_2 and CeO_2/TiO_2 of ciprofloxacin (CIP) and sulfamethoxazole (SMX), two of the main antibiotics present in water sources, has been evaluated and compared. CIP is a type of antibiotic belonging to the fluoroquinolone class, commonly used for treating bacterial infections. For instance, in one cluster of Indian pharmaceutical factories consisting of 90 bulk drug manufacturers, the effluent discharge of approximately 1500 m^3 of wastewater per day was found to contain high concentrations of ciprofloxacin, measuring 28 000 $\mu g\ L^{-1}$ and 31 000 $\mu g\ L^{-1}$ on two consecutive days, exceeding *e.g.* the levels toxic to some bacteria by over 1000-fold.[39] These concentrations correspond to the release of several kilograms of antibiotics daily and tens of tons annually into the environment. Lakes situated in the vicinity of the cluster also showed elevated levels of antibiotic contamination, with ciprofloxacin concentrations measuring up to 6500 $\mu g\ L^{-1}$,[40] while the Predicted No Effect Concentration-Minimum Inhibitory Concentration (PNEC-MIC) approach described by Bengtsson-Palme and Larsson[41] and the Antimicrobial Resistance Industry Alliance (2018)[42] has been estimated to be 0.064 $\mu g\ L^{-1}$. SMX is a sulfonamide antibiotic that was initially introduced in combination with trimethoprim by F. Hoffmann-La Roche in 1969. Despite a decline in sales figures over the past two decades, SMX continues to be widely utilized, and its PNEC has been estimated to be 0.59 $\mu g\ L^{-1}$.[43,44]

The photocatalysts used in this work have been extensively characterized by a combination of instrumental techniques including High-Resolution Transmission Electron Microscopy (HR-TEM), X-Ray Diffraction (XRD), UV-VIS spectroscopy, Dynamic Light Scattering (DLS) and BET and X-Ray Photoelectron Spectroscopy (XPS) measurements. Results show that CeO_2/TiO_2 exhibit superior photocatalytic performance, achieving complete CIP degradation within 30 and 180 minutes under UV and visible light. Remarkably, coupling TiO_2NPs with CeO_2NPs also allows the use of the hybrids at lowest reported concentrations, thus reducing the environmental impact of TiO_2NPs. The control of single component CeO_2NPs also exhibit superior photocatalytic performance in CIP degradation compared to the hybrid Au/TiO_2, which suggest that the inherent redox properties of the co-catalyst CeO_2 have an important role in the enhancement of the photocatalytic reaction. These results were further confirmed using SMX as pollutant as similar trends were observed.

2. Materials and methods

2.1. Materials and reagents

All the nanomaterials employed in this work were synthesized in the aqueous phase, using Milli-Q grade water. All reagents were purchased from Sigma-Aldrich (99% purity grade unless indicated otherwise) and used as received. Gold(III) chloride trihydrate ($HAuCl_4 \cdot 3H_2O$, CAS No. 16961-25-4) was used as precursor of AuNPs, cerium(III) nitrate hexahydrate ($Ce(NO_3)_3 \cdot 6H_2O$, CAS No. 15878-77-0) as precursor of CeO_2NPs and titanium tetrachloride ($TiCl_4$, CAS No. 7550-45-0) as precursor of TiO_2NPs. Other reagents utilized for the synthesis of the nanomaterials include sodium borohydride ($NaBH_4$, CAS No. 16940-66-2), trisodium citrate dihydrate (CAS No. 6132-04-3), potassium carbonate (K_2CO_3, CAS No. 584-08-7) and ammonium hydroxide (NH_4OH, 28% NH_3 in H_2O, ≥99.99%, CAS No. 1336-21-6). The structure of model antibiotic molecules Ciprofloxacin (CIP) and Sulfomethoxazole (SMX) are illustrated in Fig. S1† and their physio-chemical data listed in Table S1.†

2.2. Synthesis of single component Au, CeO_2 and TiO_2 NPs

All the synthesis procedures are based in pre-existed ones available in the scientific literature with few modifications to be adapted for the concentrations needed for this work. AuNPs were synthesized following the procedure based on Jana *et al.*[45] which consist on the fast injection of 0.1 M sodium borohydride (ice-cold freshly prepared) into an aqueous solution containing 0.25 mM Gold(III) chloride trihydrate and 0.25 mM trisodium citrate. This solution was kept under stirring for three hours and stored in the fridge for subsequent experiments. CeO_2NPs were synthesized by the chemical precipitation of $Ce(NO_3)_3 \cdot 6H_2O$ in a basic aqueous solution following a procedure described in Zeng *et al.*[46] Briefly, 10 mM of $Ce(NO_3)_3 \cdot 6H_2O$ was dissolved in 100 mL of Milli-Q water at room temperature. Afterward, 3 mL of 1 M ammonium hydroxide was added slowly at room temperature under vigorous stirring and the mixture was allowed to continue under mild stirring overnight. TiO_2NPs synthesis was based in the method described by Pottier *et al.*,[47] the synthesis procedure consists on the decomposition of titanium tetrachloride ($TiCl_4$) at acidic pH = 5. Subsequently, the nanocrystals were left to in an oven at 60 °C for 12 hours and purified by centrifugation steps.

2.3. Synthesis of CeO_2/TiO_2 and Au/TiO_2 hybrid photocatalysts

The hybrid nanostructures were prepared by facile and entirely hydrophilic and open atmosphere synthesis methods. The preparation of CeO_2/TiO_2 involved the following steps: first, 90 mL of the as-prepared TiO_2NPs (5 mg mL^{-1}) were mixed with 10 mL of NH_4OH at 75 mM and sonicated during 10 minutes to ensure that TiO_2NPs were fully dispersed. Second, 108.5 mg of $Ce(NO_3)_3 \cdot 6H_2O$ were stirred into the mixture and heated under reflux at 100 °C for 4 hours. Finally, the resulting solution was washed by purification and colloidally stable CeO_2/TiO_2 were redispersed in a solution of 1 mM NH_4OH. The preparation of the Au/TiO_2 involved the following steps. First, 96 mL of the as-prepared AuNPs were adjusted to pH 10 by adding equal amounts of sodium citrate and K_2CO_3 at 150 mM. This solution was heated to 90 °C under stirring. Second, 4 mL of TTIP (10 mM) was added to the solution and heating was continued for 2 hours. Similar as the CeO_2/TiO_2, the resulting solution was washed by purification and colloidally stable Au/TiO_2 were redispersed in a solution of 1 mM NH_4OH.

2.4. Characterization techniques

Nanomaterials were visualized using a high-resolution transmission electron microscopy (HR-TEM, FEI Talos, F200s). 40 μL of the colloidal solutions were drop-casted onto a carbon coated 200 mesh copper grid and left to dry at room temperature. Particle size distribution was measured using Image J Analysis software. Hydrodynamic diameters were determined with Dynamic Light Scattering (DLS, Nanotrac wave II, Macchique, USA) with a light source wavelength of 532 nm and fixed scattering angle of 173°. Measurements were conducted in 1 cm path cell and three independent measures were performed. The study of the crystallinity and structural phase of the nanomaterials was performed with a X-ray diffraction (XRD, Rigaku SmartLab SE diffractometer, Tokyo, Japan) using Cu Kα (λ = 0.15418 nm) in the range of 2θ = 5–90° with an increment of 0.02°. To identify the Ti (2p), O (1s) and Ce (3d) peaks, X-ray photoelectron spectroscopy (XPS) was measured with the Thermo Scientific K-Alpha X-ray photoelectron spectrometer (Thermo Fisher Scientific (China) Co., Ltd.) with Al Kα monochromator as an X-ray source. Nitrogen sorption isotherms were measured with a ASAP2010 analyzer (Micromeritcs, USA). Before measurements, the samples were dried in a vacuum oven at room temperature for 24 h, and outgassed in the instrument at 60 °C for 24 h. The specific surface areas were calculated by the Brunauer–Emmett–Teller (BET) method and the pore size distributions were derived from the adsorption branches of the isotherms using the Barrett–Joiner–Halenda (BJH) method. The optical properties of the photocatalysts were analyzed with UV-Visible Spectrophotometry (UV-VIS), recorded with a Shimadzu UV-1900 (Japan) spectrophotometer. 1 mL of nanomaterials or the solution containing CIP or SMX mixed with the nanomaterials were added to a quartz cuvette and spectra were achieved with scanning in the wavelength range from 190–700 nm. Table S1† list the characteristics of all nanomaterials employed as described in main text.

2.5. Photocatalytic degradation of CIP and SMX

The hybrid and single component nanomaterials were evaluated for the photocatalytic degradation of CIP and SMX both under UV and sunlight. For the degradation experiments under UV light, the artificial irradiation was provided by a 8 W lamp emitting at 365 nm (UV-A) and positioned in top of a quartz reactor (black box, ZF-IB, Shanghai Hannuo Instruments CO., Ltd. Shanghai, China) and maintained at a fixed distance of 5 cm from the samples. The degradation experiments under visible light were carried out at the Wuyi University (Jiangmen, China) whose GPS coordinates are 22° 35′ 53″ North and 113° 4′ 49″ East, from 12 p.m. to 4 p.m., 4 h irradiation time and with an average temperature of 27 °C. First, the solutions were equilibrated by stirring for 30 minutes in dark condition to achieve adsorption–desorption equilibrium before subjecting them to irradiation. The maintenance of absorbance or a slight decrease in absorbance was observed in some instances at the end of this 30 minute equilibration period, which we refer to as time = 0.[48,49] The experiments were carried out with 10 mL of 10 or 50 μg mL^{-1} of each antibiotic and a optimized concentration of 0.5 mg mL^{-1} of each photocatalyst. At different time points, the reaction mixtures were centrifuged and the concentration of remaining CIP and SMX in the supernatants were calculated by the maximum absorbance at 272 nm for CIP and 265 for SMX. The concentrations of CIP were calculated from a calibration curve using the UV-vis spectroscopy data at a wavelength of 273 nm.

3. Results and discussion

3.1. Synthesis and characterization of the CeO_2/TiO_2 and Au/TiO_2 photocatalysts

In a first set of experiments, single component Au, CeO_2, and TiO_2 NPs were synthesized and further employed for the preparation of the hybrid photocatalysts CeO_2/TiO_2 and Au/TiO_2, and as controls in the antibiotic degradation experiments. A complete synthesis description and characterization of the single component NPs used in this work can be found in previous publications from the authors[50] and in the materials and methods section. Briefly, CeO_2NPs were synthesized at room temperature by the precipitation in basic media of $Ce(NO_3)_3$, TiO_2NPs were prepared following a hydrothermal method based on the decomposition $TiCl_4$ in acidic media and AuNPs were synthesized by the reduction of $HAuCl_4$ in the presence of sodium citrate. Fig. S1† shows the Transmission Electron Microscopy (TEM) images of the as-synthesized single-component NPs and their size distributions analysed by TEM and Dynamic Light Scattering (DLS). The mean diameters of CeO_2, TiO_2 and Au NPs as determined by TEM image analysis were 5.4 ± 1.1 nm, 8.6 ± 2.1 nm and 8.6 ± 2.2 nm respectively, and their hydrodynamic diameters was 35.2 nm, 47.7 nm and

14.2 nm with narrow size distributions (polydispersity indexes of 0.1–0.2) as analysed by DLS. The increased hydrodynamic diameter in the case of the metal oxide NPs with respect to the TEM image analysis is attributed to the formation of small agglomerates in solution since the formation of the electrical double layer in metal oxide NPs is less efficient in stabilizing them compared with metal NPs.[51]

The hybrid photocatalysts were prepared by simple wet-chemistry methods. The selection of Au and CeO_2 NPs co-catalyst sizes, ranging between 5 and 10 nanometers, and the loading amount has been made based on their consistent demonstration of enhanced catalytic activity.[52,53] In the case of CeO_2/TiO_2, 100 mL of the as-prepared TiO_2NPs (5 mg mL^{-1}) were dispersed in an aqueous ammonia solution of 7.5 mM followed by 10 minutes sonication to disperse the TiO_2NPs. Afterwards, 108.5 mg of $Ce(NO_3)_3\cdot 6H_2O$ were added under stirring to obtain a concentration of Ce^{3+} precursor of 2.5 mM. This mixture was heated under reflux and maintained at 100 °C for 4 hours. The synthesis of CeO_2NPs based on the oxidation of a cerium salt (mainly nitrate or chloride) in basic conditions is common in the literature and it is known that yield monodisperse small-sized (4–5 nm) CeO_2NPs at this $Ce^{3+}:NH_4OH$ ratio of 1 : 3.[46,54,55] The resulting solution was washed by purification and colloidally stable CeO_2/TiO_2 were redispersed in a solution of 1 mM TMAOH. Fig. 1a shows TEM and high-angle annular dark field images (HAADF) of the as-synthesized CeO_2/TiO_2, which appear as agglomerated nanocomposites containing both CeO_2 and TiO_2. The HAADF corresponding elemental mapping shows that CeO_2 and TiO_2 NPs are thoroughly distributed in the hybrid structure and the inset reveals the (111) planes of face-centered cubic CeO_2 and (101) of anatase TiO_2. According to ICP-MS analysis, a 5% of CeO_2 is present in the hybrids, which is consistent with the mass of precursors added in the synthesis. For the Au/TiO_2, to ensure a good dispersion of the Au and the TiO_2 organized in a similar fashion to the CeO_2/TiO_2 hybrids, TiO_2NPs were formed onto previously synthesized AuNPs. 50 mL of the as-prepared AuNPs were adjusted to pH 10 by adding equal amounts of sodium citrate and K_2CO_3 at 150 mM. The solution was heated to 90 °C under stirring. Subsequently, 50 mL of $TiCl_4$ (20 mM) was added and the mixture was heated to boiling for 2 hours. As in the case of the CeO_2/TiO_2 hybrids, the calculated data of 5% of Au in the Au/TiO_2 hybrids is similar than ICP-MS data although slightly increased (7%), probably because not all the $TiCl_4$ precursor reacted and was washed in the purification step. Fig. 1b shows the TEM and HAADF characterization, where the higher density of metallic Au reveals the dark (bright-field TEM) or white (dark-field TEM) Au nanospheres onto a TiO_2 NPs matrix.

From the TEM images, the presence of both AuNPs and TiO_2NPs in the Au/TiO_2 hybrids is more clearly evidenced compared with CeO_2/TiO_2 hybrids thanks to the higher atomic number of Au compared with Ti. Thus, to further prove the presence of CeO_2NPs and TiO_2NPs in the CeO_2/TiO_2 hybrids, the XRD diffraction patterns of the as-synthesized single component CeO_2 and TiO_2 NPs and CeO_2/TiO_2 hybrid nanostructures were analysed (Fig. 2a and c). The XRD pattern of single component TiO_2NPs shows the diffraction peaks at 25.3°, 37.9°, 48.0°, 53.9°, 55° and 63°, which can be ascribed to the reflection of (101), (004), (200), (105), (211) and (204) planes of the TiO_2 respectively, consistent with the standard JCPDS values of anatase TiO_2 (JCPDS No. 21-1272). In the case of CeO_2NPs, the peaks at 28.6°, 33.1°, 47.5°, 56.3° can be ascribed to the (111), (200), (220) and (311) planes of fluorite (cubic) CeO_2 phase (JCPDS No 34-0394). The XRD patterns of both single component NPs exhibit well-defined peaks, although broad due to the small particle size, indicating that the materials are present in a good crystallinity phase. The crystalline sizes of CeO_2NPs (4.8 nm) and TiO_2NPs (6.08 nm) calculated from the XRD data using Scherrer's formula (taking the Full Width at Medium Height of the CeO_2 cubic (111) and anatase (101) reflections) are consistent with those obtained by TEM analysis.

In the case of CeO_2/TiO_2 the calculated crystallite size was 5.12 nm. As the peaks are rather broad, the anatase (101) reflection interfere/mask the CeO_2 cubic (111) main reflection as well as the other dominant (220) and (311) reflections. Other CeO_2 peaks are barely visible due to the low quantity of CeO_2-NPs in the hybrids. Nonetheless, the smaller crystallite size of the hybrid compared with the pure anatase TiO_2 is attributed to the broadening effect due to the incorporation of CeO_2 into the TiO_2 matrix,[36,56] and it can be noted from the lower intensity and broader width of the peaks of the hybrid compared with pure TiO_2 (Fig. 2c). Furthermore, unshifted peaks of the TiO_2NPs compared with the CeO_2/TiO_2 hybrid suggest that the TiO_2 lattices were not disturbed by the presence of Ce ions, probably because of the larger radius of Ce^{4+} (0.102 nm) than that of Ti^{4+} (0.064 nm) which make it difficult for them to enter into TiO_2 crystal lattice.[57,58] Thus, this suggests that the nanocomposites observed in TEM images are composed of CeO_2 and TiO_2 NPs. In the case of Au/TiO_2 hybrids the presence of the peaks corresponding to Au and TiO_2 can be clearly distinguished and the calculated crystalline size using Scherrer's formula of 6.17 nm was similar to the TiO_2NPs since the (101) reflection of TiO_2 is not affected by the presence of the AuNPs (Fig. S2†).

Additionally, Raman spectra were employed to further confirm the above description in the case of CeO_2/TiO_2 (Fig. 2b). Single component TiO_2NPs and TiO_2/CeO_2 hybrids show the characteristic Raman-active modes of TiO_2 anatase phase (A_{1g}, B_{1g}, E_g) which are ascribed to the 145, 196, 397, 517 and 639 cm^{-1} peaks.[59] As in the case of XRD, the peak of CeO_2NPs (464 cm^{-1}) is barely noted in the CeO_2/TiO_2, but, it can be noted the broadening and blue shift of the most intense peak in the hybrid respect with TiO_2NPs. This has been attributed to non-stoichiometric defects and non-homogeneity of particle size distribution due to the presence of the CeO_2NPs,[36,60] which is consistent with the XRD results.

Further, X-ray photoelectron spectroscopy (XPS) was employed to analyse the chemical composition and chemical state of elements in the CeO_2/TiO_2 hybrids. Fig. 2d–g shows the high-resolution XPS spectra of Ti 2p, Ce 3d, and O 1s in the CeO_2/TiO_2. In the survey plot (Fig. 2d) the presence of four main elements Ti, O, Ce, and C can be observed. The presence of C is common in XPS analysis due to contamination from environmental air during sample preparation. The peaks at 530 and 532 eV are assigned to O^{2-} ion in the TiO_2 crystal structure and

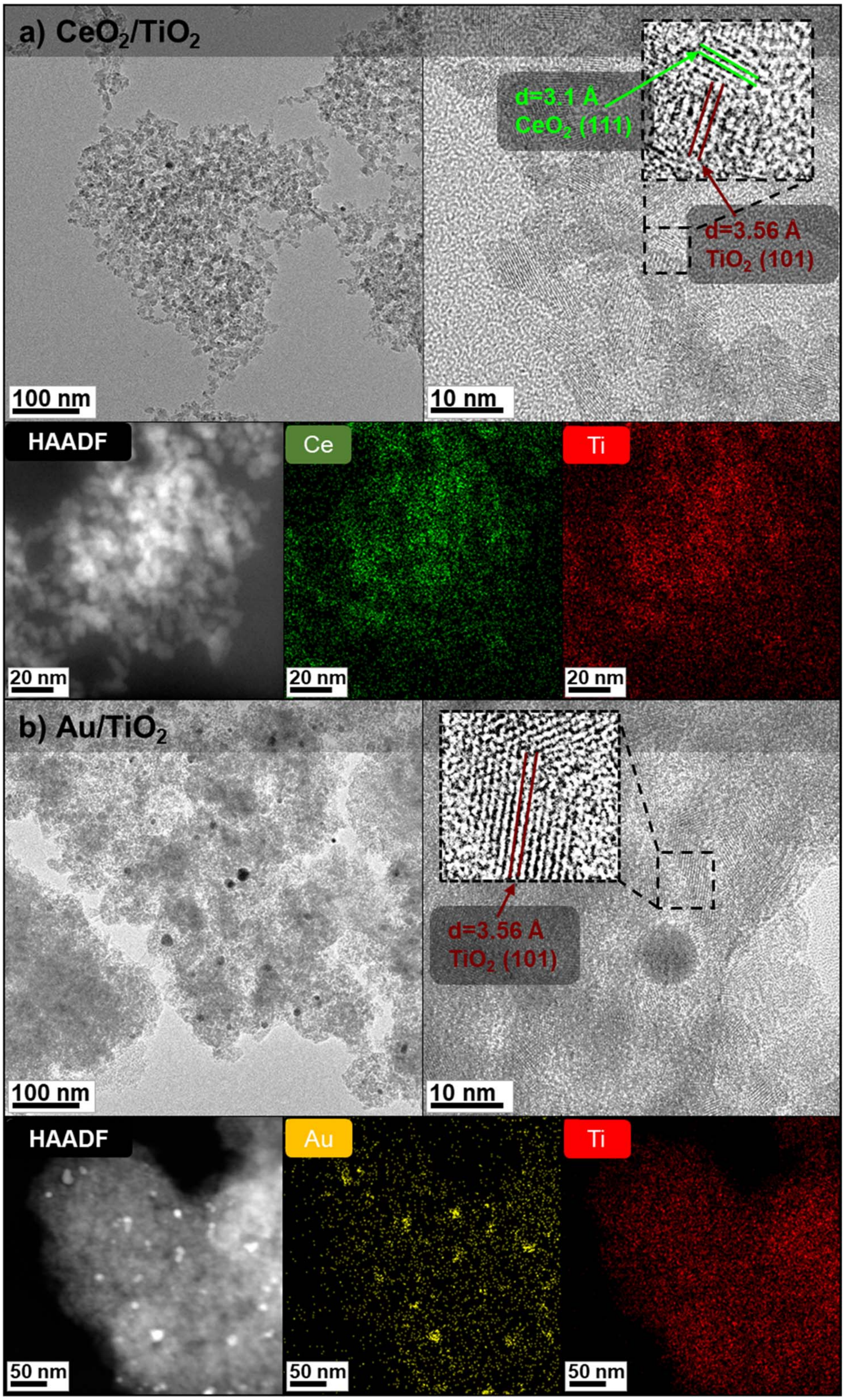

Fig. 1 Morphology of the CeO_2/TiO_2 (a) and Au/TiO_2 (b) hybrid nanostructures. For each hybrid, upper rows show representative TEM images and lower rows the high-angle annular dark field TEM (HAADF-TEM) images revealing the formation of both $CeO_2$and TiO_2 in the CeO_2/TiO_2 and Au and TiO_2 in the Au/TiO_2. Inset in (a) shows the (111) planes of face-centered cubic CeO_2 phase and (101) of anatase TiO_2 and inset in (b) the (101) of anatase TiO_2.

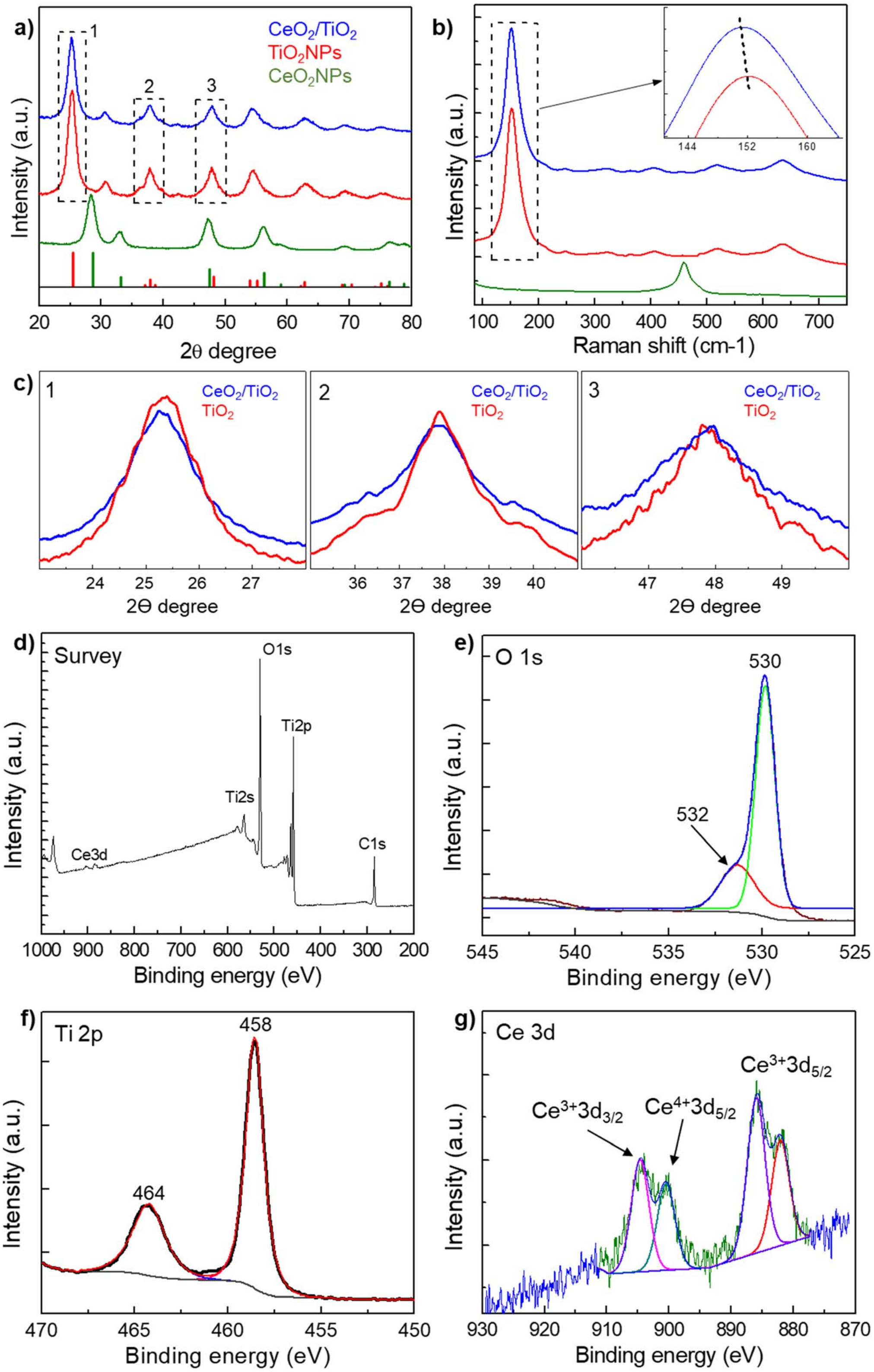

Fig. 2 Physicochemical characterization of the CeO_2/TiO_2 hybrid nanostrucutures. (a) XRD patterns of the CeO_2 and TiO_2 NPs and the CeO_2/TiO_2 hybrid. (b) Raman spectra of the CeO_2 and TiO_2 NPs and the CeO_2/TiO_2 hybrid. Inset is the predominant peak of TiO_2 which is blue-shifted in the CeO_2/TiO_2 hybrid. (c) Details of the anatase TiO_2 and CeO_2/TiO_2 hybrid diffraction peaks at around 25° (1), 38° (2) and 48.0° (3). (d–g) XPS analysis of the CeO_2/TiO_2 including survey spectra (d), O 1s core-level spectra (e), Ti 2p core-level spectra (f) and Ce 3d core-level spectra (g).

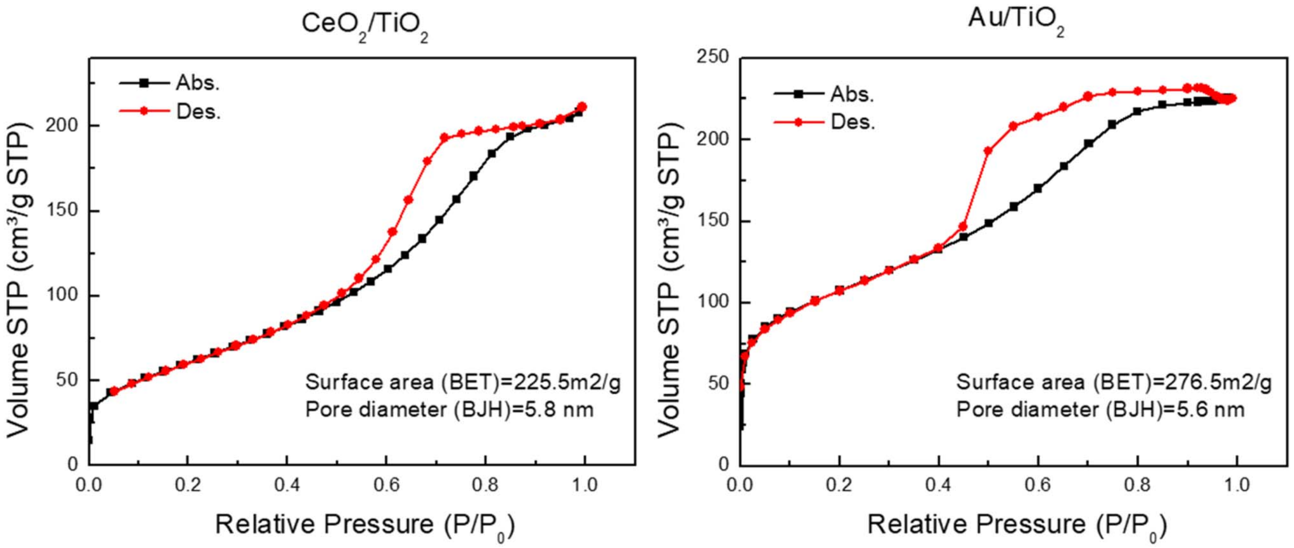

Fig. 3 Nitrogen sorption isotherms and textural properties of the CeO_2/TiO_2 (left) and the Au/TiO_2 (right) hybrid nanostrucutures.

Ti–OH bond (Fig. 2e). The dominant peak located at 530 eV has been described as characteristic of metal oxides arising from the lattice of CeO_2 and TiO_2.[61] The Ti 2p core-level spectrum (Fig. 2f) shows two major peaks at 458.4 and 464.2 eV, corresponding to the Ti $2p_{3/2}$ and Ti $2p_{1/2}$ spin–orbit split photoelectrons of Ti^{4+} respectively, which is characteristic of TiO_2 species. In the case of Ce, the 4f group is particularly complex because of its associated peak structure. The Ce3d core-level spectrum (Fig. 2g) shows different groups of peaks. One group of two peaks at 882 eV corresponds to the Ce^{3+} $3d_{5/2}$ spin orbital and another group of two peaks around 900 eV corresponds to the Ce^{4+} $3d_{5/2}$ (898 eV) and Ce^{3+} $3d_{3/2}$ (904 eV).[62,63] In both cases, the peaks are asymmetric, which is attributed to the mixture of Ce^{3+} and Ce^{4+} in the CeO_2NPs structure.[57,64–66] Furthermore, based on the non-linear least squares fitting of CeO_2 synthesized as in the hybrids, compostion of Ce^{3+} and Ce^{4+} were found to be 65.1% and 34.9% respectively. The presence of both Ce^{4+} and Ce^{3+} in the CeO_2 from the CeO_2/TiO_2 hybrids is important since it improves the electron transfer characteristics and the separation efficiency of photogenerated electrons and holes, and consequently it is expected it will improve the photocatalytic activity with respect to pure TiO_2.

Finally, nitrogen adsorption/desorption measurements were performed on the CeO_2/TiO_2 and Au/TiO_2 hybrid nanostructures to determine their specific surface area and textural properties. Fig. 3 displays the isotherms, revealing that both photocatalysts exhibited a characteristic type-IV isotherm, as per the IUPAC classification. This observation indicates a well-developed mesoporous structure. The BET surface area and average pore diameter determined from the adsorption branch using the BJH method for CeO_2/TiO_2 were 225.5 $m^2\ g^{-1}$ and 5.8 nm, respectively. Meanwhile, for Au/TiO_2, these values were 276.9 $m^2\ g^{-1}$ and 5.6 nm. This suggests that the obtained hybrids share similar characteristics, not only in terms of size and co-catalyst doping but also in morphology and surface area and that the coupling of CeO_2 or Au NP lead to similar hybrid structures.

3.2. Optical properties of the CeO_2/TiO_2 and Au/TiO_2 photocatalysts

The optical properties of both CeO_2/TiO_2 and Au/TiO_2 were investigated by UV/VIS spectroscopy. Fig. 4a shows the UV/VIS spectra for both CeO_2/TiO_2 and Au/TiO_2, along with the single component NPs, which confirm the presence of the single component NPs in both hybrids. Furthermore, it can be observed that compared with pure TiO_2, both hybrid structures display an extension of their UV/VIS absorbance to the visible light region. Next, the band gap energy (E_g) values of the single component and hybrid nanostructures were determined by fitting the UV/VIS data with Tauc's plots[67,68] following the developments by Davis and Mott for amorphous semiconductors,[69] and later by many others. It is worth noting that the linear extrapolation to zero in the plots of $(\alpha h\nu)^2$ *versus* photon energy to estimate E_g values, is a common approach for providing a rough approximation of the direct band gap. This is because the Tauc plot method assumes measurements under specific conditions, potentially introducing uncertainties.[70] Additionally, variations in the data or the choice of the linear fitting range can impact the accuracy of the estimated bandgap. The E_g values for TiO_2, CeO_2, Au/TiO_2 and CeO_2/TiO_2 are 3.52, 3.55, 3.34 and 3.01 eV respectively (Fig. 4b). The E_g is lower in the hybrids compared with the single component NPs which confirms again the incorporation of both Au and CeO_2 in the TiO_2 matrix to form the hybrid nanostructures.

Importantly, the decrease of E_g values in the hybrids compared with TiO_2NPs is an indication of the red shifting from UV to the visible region. Therefore, it can be hypothesized that this will enable the photocatalytic activity under sun irradiation. This can be explained by the electronic band structure in the hybrids. CeO_2 is a p-type semiconducting photocatalyst material with potentially suitable band positions for the promotion of charge carriers when kept in intimate connection with TiO_2. When electrons in the CeO_2 valence band are exposed to lower energy lights (*e.g.* visible light) they move to the conduction

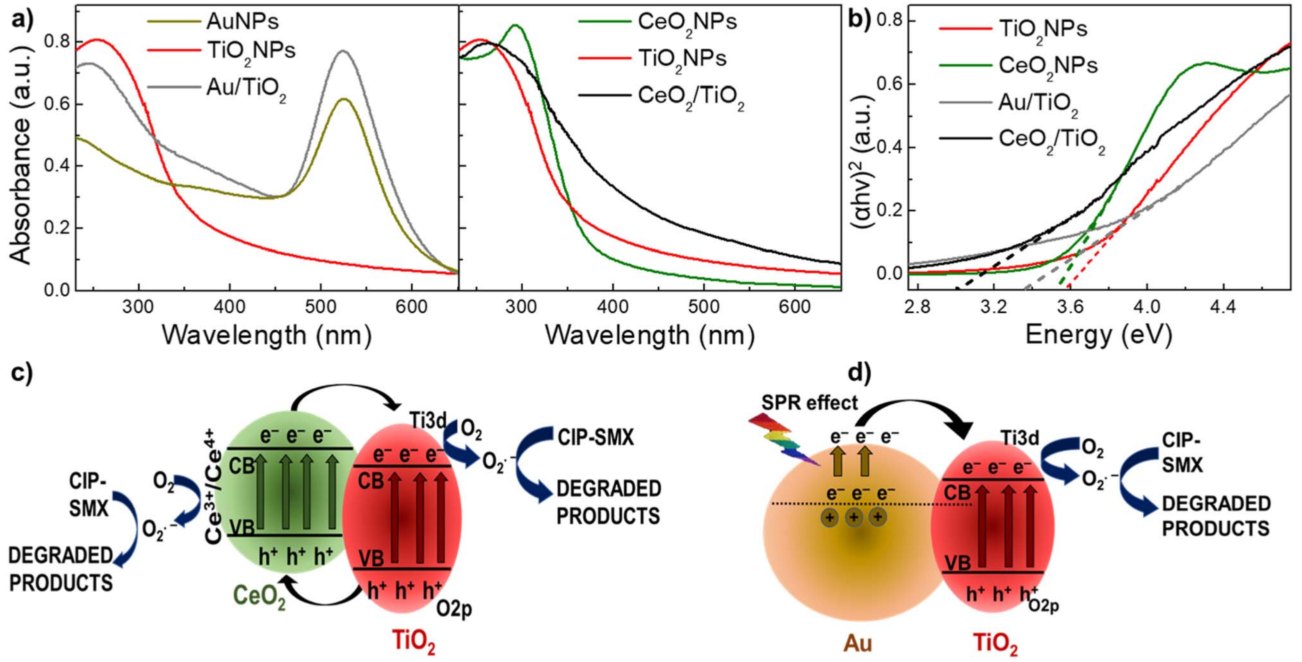

Fig. 4 Optical properties of the CeO_2/TiO_2 and Au/TiO_2 hybrid nanostrucutures. (a) UV/VIS spectra of both hybrids along with the single component NPs. (b) Corresponding Tauc plots which represent the square of the absorption coefficient *versus* photon energy. The bandgap energy (E_g) of the material can be determined from the *x*-axis intercept of the linear portion of the curve. (c and d) Schematic diagram of the proposed mechanism for the photocatalysis by CeO_2/TiO_2 (c) and Au/TiO_2 (d) under visible light irradiation. The different band structures of the co-catalysts respect TiO_2 facilitate the transfer of electrons to the TiO_2 conduction band (CB), and subsequently from the CB of TiO_2 to oxygen molecules, resulting in the formation of superoxide radicals ($O^{2\bullet-}$). Furthermore, the co-catalysts facilitate the regeneration of the CB of TiO_2 and act as a trap for the photo-generated holes, preventing their recombination with electrons and prolonging the lifetime of the charge carriers, thus potentially enhancing the photocatalytic activity. Additionally, CeO_2NPs can undergo oxidation reactions by themselves.

band. As a result of the varied energy barriers of both components in the hybrids, electrons will eventually relocate to the conduction band of TiO_2.[36,71] Further, electrons in the TiO_2 valence band will also undergo excitation when exposed to higher energy light (*e.g.* UV which accounts for the 4% of the sun irradiation), and the hole in its valence band will shift to the CeO_2 valence band. This carrier transport process efficiently separates photoelectrons and holes, making their recombination more difficult and broadening the response to visible light.[71] Au/TiO_2 is most well-described in the literature. In such nanostructures, due to SPR in the Au surface, electrons from the AuNPs conduction band become excited (known as hot electrons) under visible light irradiation. These charge carriers are relocated from the excited AuNPs to the conduction band of the adjacent TiO_2, since there is close contact between the surfaces of Au and TiO_2 (known as Schottky junction). This movement generates holes in the AuNPs electronic structure and achieves a similar effect as described in the CeO_2/TiO_2, making electron–hole recombination more difficult. Thus, with the efficient supply of hot electrons TiO_2 can undergo the photocatalytic reaction under light illumination.[12,27,28,72] Fig. 4c and d shows a scheme of these carrier transport processes under visible light of CeO_2/TiO_2 and Au/TiO_2 hybrid nanostructures.

3.3. Degradation of CIP and SMX

All material improvements of the Au/TiO_2 and CeO_2/TiO_2 hybrids described in the previous sections compared with the single component NPs were evaluated and compared in the context of CIP and SMX degradation. First, the concentration of the photocatalysts to be used in the degradation experiments was determined. This is important since increasing the concentration of a photocatalyst can increase its photocatalytic activity up to a point where the solution becomes turbid due to a high concentration of particles, which reduces the penetration of the light (effect known as catalyst shielding). In addition, the high catalyst concentration may also block access to the catalytic sites because of the agglomeration of the particles. The effect of catalyst concentration on the degradation of Rhodamine B (RhB) and CIP with TiO_2NPs was studied. First, varying concentration of TiO_2NPs were used for the degradation of RhB at initial concentration of 2.5 mM (Fig. S3†). From these studies, 0.5 mg mL^{-1} of photocatalyst was selected as optimized concentration, which is a similar result than the previously reported for TiO_2 and Au/TiO_2 for RhB degradation.[72,73] Next, we used 0.5 mg mL^{-1} of CeO_2/TiO_2 and Au/TiO_2 hybrids (and TiO_2, CeO_2 and Au single component NPs as controls) to corroborate its suitability for the degradation of 10 μg L^{-1} of CIP.

Fig. 5a shows the kinetic plots of CIP degradation, where CeO_2, TiO_2 and the CeO_2/TiO_2 hybrids showed 100% CIP degradation (although at different time points in each case). This concentration of photocatalysts was used with further experiments under sun irradiation (Fig. 5a) and with an at an increased CIP concentration of 50 μg L^{-1} (Fig. 5b). The CIP[48,74] and SMX[75,76] degradation pathways and degraded products

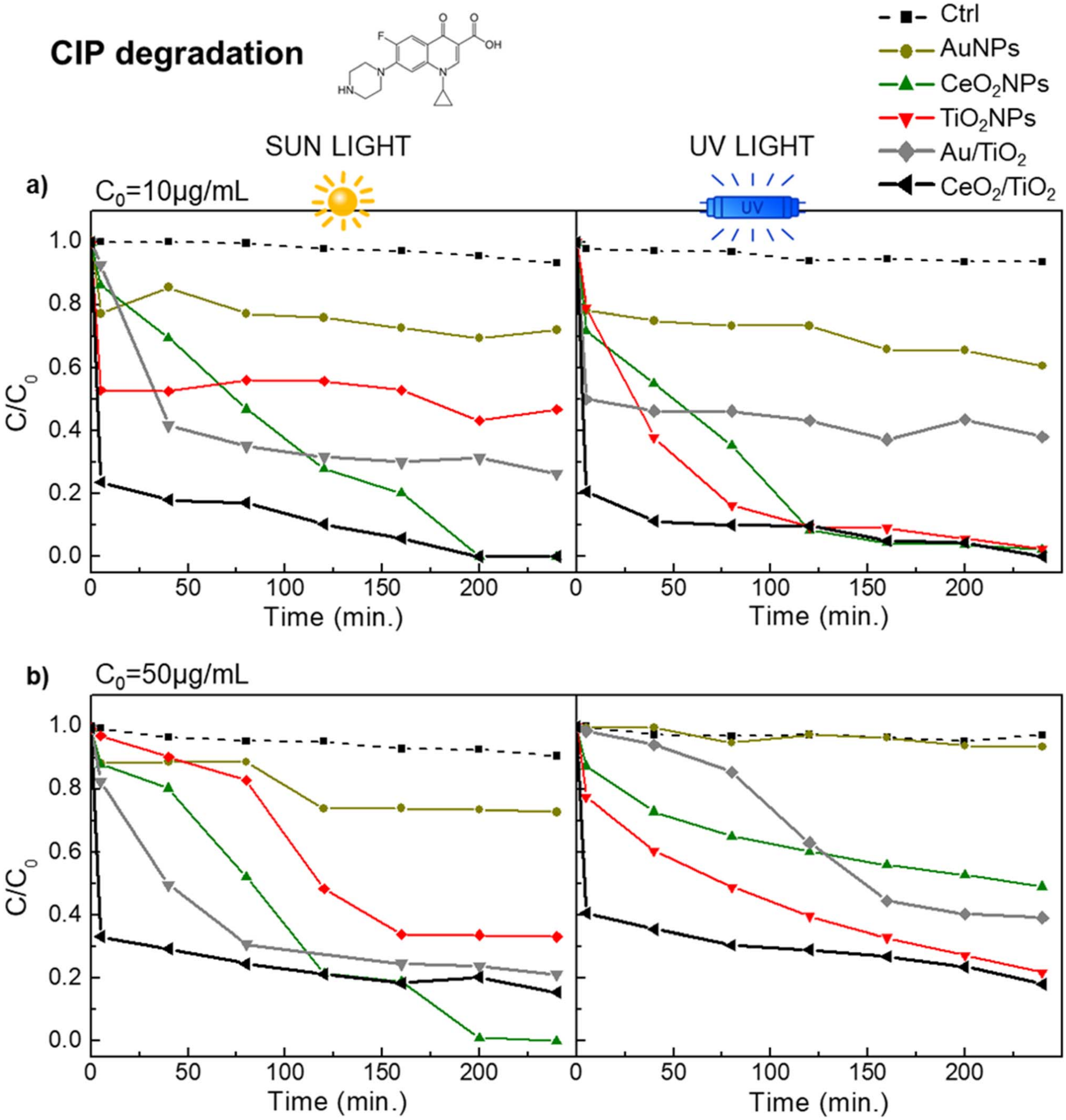

Fig. 5 Photocatalytic performance in the degradation of CIP of the hybrid CeO_2/TiO_2, Au/TiO_2 and single component NPs under visible and UV light. (a) CIP initial concentration of 10 μg mL; (b) CIP initial concentration of 50 μg mL^{-1} (b). Black and grey line correspond to CeO_2/TiO_2 and Au/TiO_2 hybrids respectively. Yellow line is AuNPs, green line is CeO_2NPs, red line is TiO_2 NPs and dashed line correspond to the control (H_2O). All photocatalysts were used at a concentration of 0.5 mg mL^{-1}. The control group (ctrl) consists of the antibiotic dissolved in a water solvent. The molecular structure of CIP is in Fig. S1.†

using TiO_2NPs and hybrid TiO_2-based photocatalysts both under UV and sun irradiation have been reported elsewhere, as well as the toxicity of the resulting degradation products. For instance, in the case of CIP, Durán-Álvarez *et al.*[77] reported negligible toxicity towards *Vibrio fischeri* and the complete removal of antibiotic activity against *Escherichia coli* when employing TiO_2 modified with metallic NPs at an initial CIP concentration of 30 μg mL^{-1}. This was attributed to the complete mineralization of CIP following 360 minutes of photocatalytic treatment under simulated sunlight irradiation. Similarly, Zheng *et al.*[78] obtained comparable results using TiO_2-based nanocomposites at an initial CIP concentration of 30 μg mL^{-1}. Regarding SMX, among others, Borowska *et al.*[76] reported the decrease of phytotoxicity of SMX degraded

Table 1 Degradation of CIP and SMX (%) using the synthesized photocatalysts at 0.5 mg mL^{-1}

	CIP degradation (%)				SMX degradation (%)			
	C_o(CIP)		C_o(CIP)		C_o(SMX)		C_o(SMX)	
	10 μg mL^{-1}		50 μg mL^{-1}		5 μg mL^{-1}		10 μg mL^{-1}	
	SUN	UV	SUN	UV	SUN	UV	SUN	UV
AuNPs	27.8	39.4	27.2	65.2	21.7	20.3	25.4	8.9
CeO_2NPs	99.9	97.8	99.9	50.9	69.5	40.6	78.8	23.8
TiO_2NPs	53.2	97.5	66.8	78.2	34.6	65.1	29.4	66.1
Au/TiO_2	73.7	61.9	78.8	60.9	56.7	42.2	49.2	32.8
CeO_2/TiO_2	99.9	99.9	84.6	81.8	87.7	84.2	67.7	32.5

products towards the plant *Lepidium sativum* when using TiO_2NPs doped with noble metals at an initial SMX concentration of 1 μg mL^{-1}. This low phytotoxicity was attributed to the very low concentrations of remaining antibiotics. Gong *et al.*[79] also observed a significant reduction in toxic activity against the green alga *Chlorella vulgaris* and the brine shrimp *Artemia salina* after photodegradation of SMX under UV radiation.

In all cases, a similar pattern can be observed. CeO_2/TiO_2 hybrids consistently show the highest CIP degradation rate compared to the other nanomaterials. Specifically, at a CIP concentration of 10 μg L^{-1}, both CeO_2/TiO_2 and CeO_2NPs showed complete degradation under UV and sun irradiation while TiO_2NPs show 100% degradation under UV light and 50% degradation under sun irradiation. In the case of the CeO_2/TiO_2 hybrids, the degradation was found to be constant after 40 min of reaction time, while for other nanomaterials it took around 2 hours to reach the stability, suggesting a more powerful activity of the CeO_2/TiO_2 in all conditions. As expected, Au/TiO_2 hybrids also enhanced the photocatalytic activity of TiO_2 under sun irradiation, although to a lesser extent than CeO_2/TiO_2 (around 75% CIP degradation in the case of Au/TiO_2 while 50% degradation was observed in the case of TiO_2 at an initial concentration of CIP of 10 μg mL^{-1}), and AuNPs showed less than 20% CIP degradation in those conditions. Table 1 shows the percentage of CIP degradation in all cases.

Remarkably, the amount of photocatalyst used was lower than many other studies also aimed to study the degradation of CIP by nanostructured photocatalysts. Among others (see Table 2 for full list), Manasa *et al.*,[48] employing 1 mg mL^{-1} of Ce-doped TiO_2NPs achieved 93% CIP degradation at C_0 = 10 μg mL^{-1}. Pattnaik *et al.*[80] employing exfoliated graphitic carbon nitride (g-C_3N_4) found that the same 1 mg mL^{-1} concentration of photocatalyst degraded up to 78% of a 20 μg mL^{-1} CIP solution exposed to solar light. Yu *et al.*,[81] employing Zn-doped Cu_2ONPs at 0.6 mg mL^{-1} achieved 94.6 CIP degradation at C_0 = 20 μg mL^{-1}. Furthermore, Gad-Allah *et al.*,[82] used 1.5 mg mL^{-1} of TiO_2NPs to efficiently degrade CIP at C_0 = 50 μg mL^{-1}, in this case using simulated sunlight.

These results were further corroborated with the photocatalytic degradation of SMX in the same conditions as the used

Table 2 Degradation of CIP by different nanostructured photocatalysts under visible light

	Concentration of photocatalyst (mg mL^{-1})	CIP initial concentration (μg mL^{-1})	CIP degradation
TiO_2-based photocatalysts			
TiO_2NPs (under simulated sunlight)[82]	1.5 mg mL^{-1}	50 μg mL^{-1}	99.9%
P25–TiO_2 (ref. 83)	1 mg mL^{-1}	20 μg mL^{-1}	31%
P25–TiO_2 (ref. 84)	1.5–11 mg mL^{-1}	30 μg mL^{-1}	99%
Immobilized TiO_2NPs[85]	1 mg mL^{-1}	3 μg mL^{-1}	92.8%
Immobilized TiO_2NPs[86]	7.5 mg mL^{-1}	20 μg mL^{-1}	95%
Au–TiO_2, Ag–TiO_2 and Cu–TiO_2 (ref. 77)	1.5 mg mL^{-1}	30 μg mL^{-1}	99%
Hybrid TiO_2:Au nanostars[87]	1 mg mL^{-1}	5 μg mL^{-1}	89%
Ce-doped TiO_2 (ref. 48)	1 mg mL^{-1}	10 μg mL^{-1}	93%
g-C_3N_4/TiO_2 powder[49]	1 mg mL^{-1}	10 μg mL^{-1}	95%
Chlorophyll sensitized TiO_2NPs[88]	0.75 mg mL^{-1}	10 μg mL^{-1}	75%
Other materials			
MnO_2 (ref. 89)	7 mg mL^{-1}	10 μg mL^{-1}	90%
		20 μg mL^{-1}	60%
Pt/$InVO_4$	3 mg mL^{-1}	20 μg mL^{-1}	87%
Pt–$BiVO_4$ (ref. 90)	1.5 mg mL^{-1}	10 μg mL^{-1}	92%
Exfoliated g-C_3N_4 (ref. 80)	1 mg mL^{-1}	20 μg mL^{-1}	78%
Zn-doped Cu_2O[81]	0.6 mg mL^{-1}	20 μg mL^{-1}	94.6%
N–ZnO/CdS/GO[91]	0.5 mg mL^{-1}	15 μg mL^{-1}	85%
CeO_2/CdS/RGO[92]	0.5 mg mL^{-1}	40 μg mL^{-1}	90%
N doped-graphene quantum dots-$BiVO_4$/gC_3N_4 (ref. 93)	0.5 mg mL^{-1}	10 μg mL^{-1}	72%
CeO_2/ZnO nanocomposites[94]	0.25 mg mL^{-1}	15 μg mL^{-1}	60%
Reduced graphene oxide-$BiVO_4$ (ref. 95)	0.2 mg mL^{-1}	10 μg mL^{-1}	68.2%
This study			
CeO_2–TiO_2	0.5 mg mL^{-1}	10 μg mL^{-1}	99.9%
CeO_2–TiO_2	0.5 mg mL^{-1}	50 μg mL^{-1}	85%

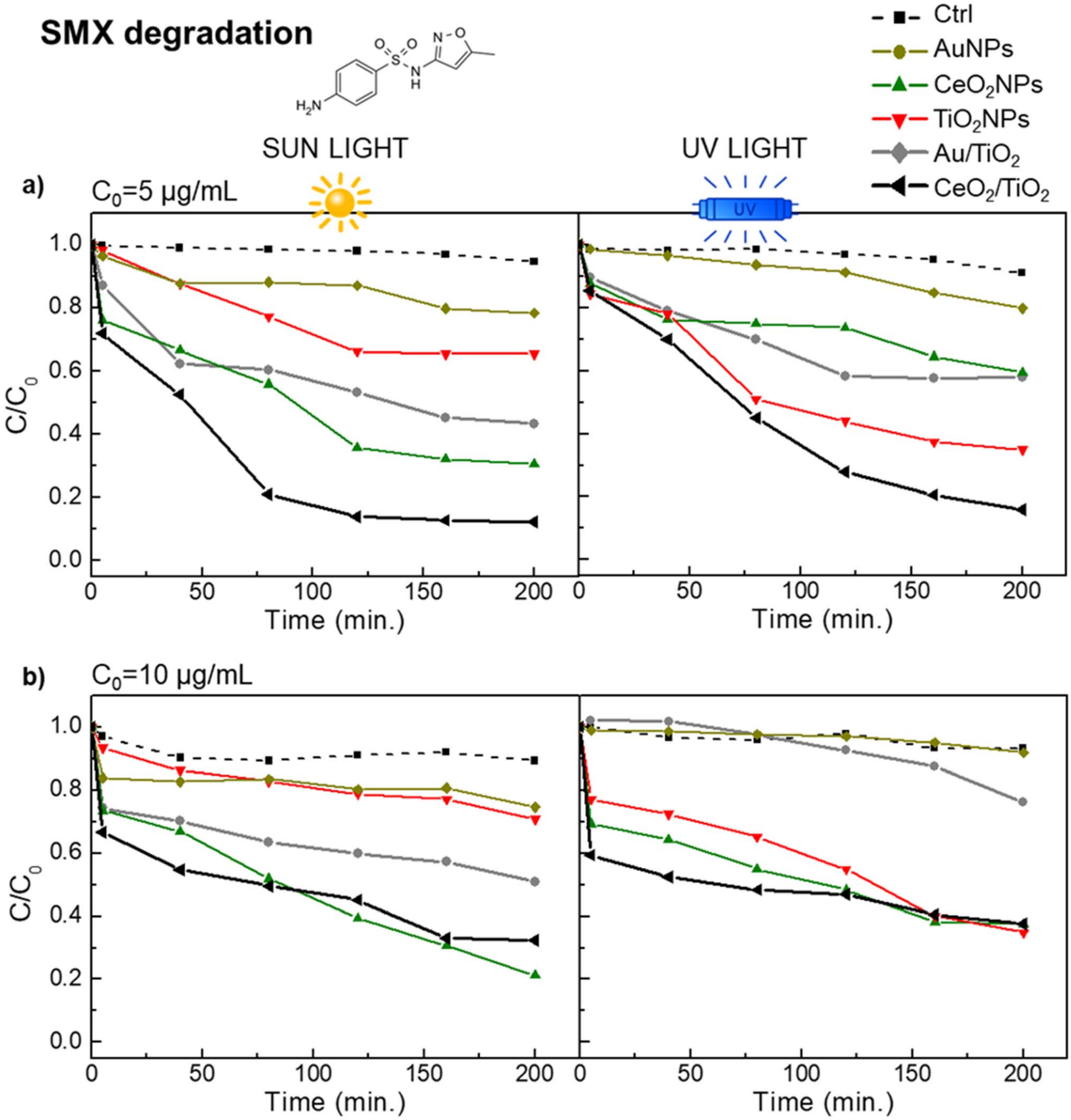

Fig. 6 Photocatalytic performance in the degradation of SMX of the hybrid CeO_2/TiO_2, Au/TiO_2 and single component NPs under visible and UV light. (a) SMX initial concentration of 5 μg mL; (b) SMX initial concentration of 10 μg mL^{-1} (b). Black and grey line correspond to CeO_2/TiO_2 and Au/TiO_2 hybrids respectively. Yellow line is AuNPs, green line is CeO_2NPs, red line is TiO_2 NPs and dashed line correspond to the control (H_2O). All photocatalysts were used at a concentration of 0.5 mg mL^{-1}. The control group (ctrl) consists of the antibiotic dissolved in a water solvent. The molecular structure of SMX is in Fig. S4.†

for the CIP degradation. Fig. 6 shows a similar pattern of SMX degradation as observed in the CIP degradation experiments. CeO_2/TiO_2 exhibited superior and faster catalytic performance under UV and sun irradiation than other photocatalysts. Note that to achieve 100% SMX degradation, a lower concentration than in case of CIP degradation was needed (initial SMX concentrations of 5 μg L^{-1} and 10 μg L^{-1}), probably due to the different molecular structures of both antibiotics and that the system was optimized for CIP. Specifically, at SMX C_0 = 5 μg mL^{-1} and under sun irradiation, CeO_2/TiO_2 showed the highest degradation (88%) followed by CeO_2NPs (70%) and Au/TiO_2 (57%) CeO_2 and TiO_2 NPs (*c.a.* 35%). At SMX C_0 = 10 μg mL^{-1}, suggesting once again the importance of the CeO_2 co-catalyst properties for photocatalytic reactions under visible light.

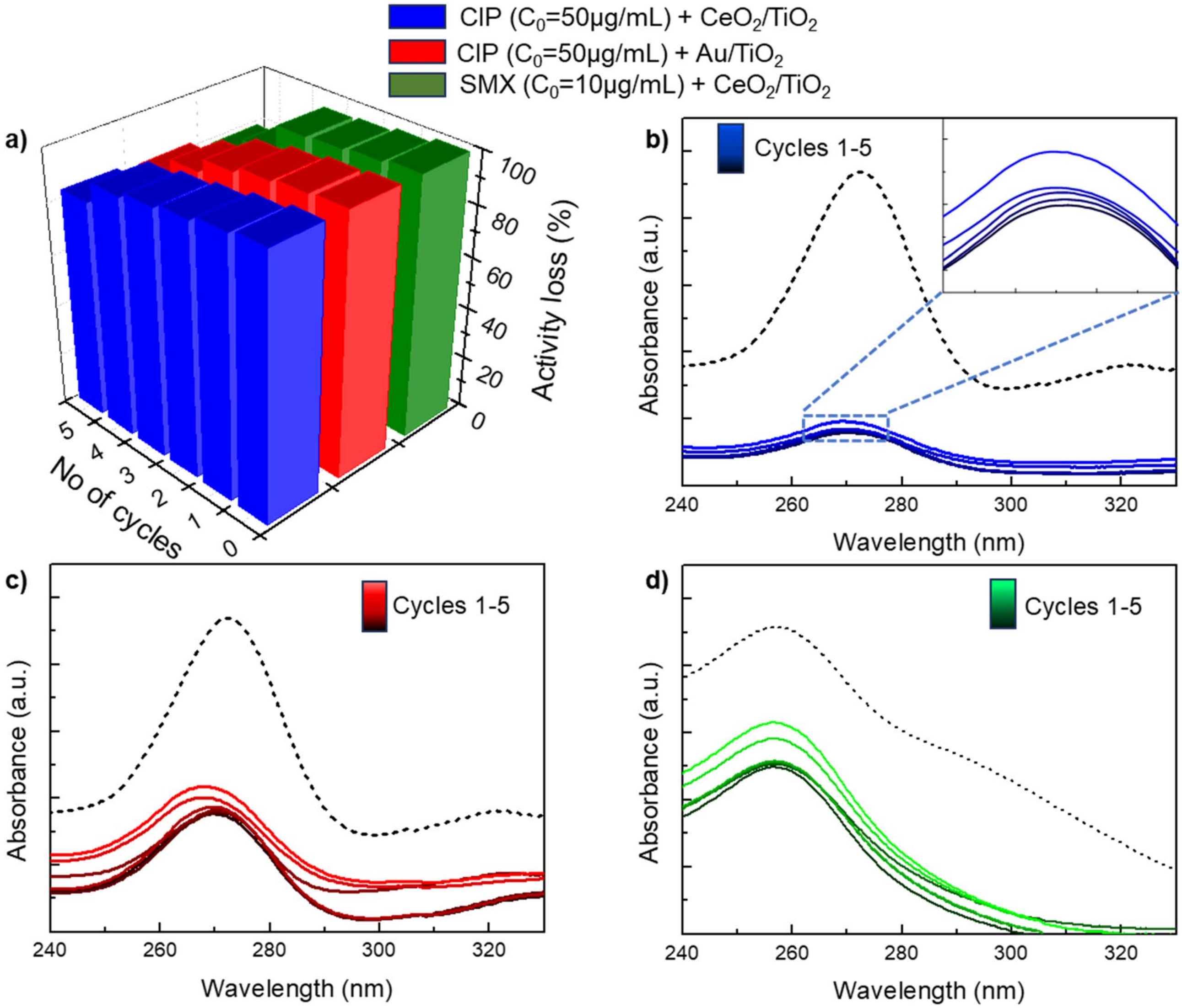

Fig. 7 Stability studies of the CeO$_2$/TiO$_2$ and Au/TiO$_2$ photocatalysts under sun irradiation. (a) Degradation of CIP or SMX at 50 µg mL^{-1} in different cycles of recovering the hybrids from the solution compared with the degradation showed by the as-synthesized hybrid nanocomposites. (b) UV-VIS absorbance of CIP (dashed line; peak at 272 nm) and with different cycles exposed to CeO$_2$/TiO$_2$. (c) UV-VIS absorbance of CIP and under the different cycles exposed to Au/TiO$_2$. (d) UV-VIS absorbance of SMX (dashed line; peak at 265 nm) and with different cycles exposed to CeO$_2$/TiO$_2$.

Interestingly, in a specific case, at the highest initial concentration of antibiotics (50 µg mL^{-1} of CIP and 10 µg mL^{-1} of SMX), CeO$_2$NPs exhibited a higher rate of degradation compared to the CeO$_2$/TiO$_2$ hybrids. It is important to note here that, even though the hybrids possess a greater surface area at the same mass concentration (Table S1†), in the experimental setup the single-component NPs have higher colloidal stability and, consequently, enhanced mobility in solution. This disparity in colloidal behaviour may account for the observed increase in catalytic activity.

In any case, the results altogether and the fact that CeO$_2$ itself also showed efficient photocatalytic activity in the degradation of CIP, suggest the superior capability of CeO$_2$ as a co-catalyst which can be attributed to its unique redox properties and its characteristic d and f electronic orbital configurations,[96–99] along with other advantages such as the reported visible active band gap value, large oxygen storage capacity, and its variable oxidation states (Ce^{3+}, Ce^{4+}) which favor electron transfer and improve the electron–hole separation. This non-stoichiometry of CeO$_2$ has also been related with its capacity to store oxygen and release them in oxidation reactions for *e.g.* the photocatalytic degradation of organic and pharmaceutical pollutants.[97,100–102] Apart from their inherent ability to initiate photocatalytic reactions by themselves, it has been reported that Ce^{4+} ions in the CeO$_2$ crystal structure can easily capture photogenerated electrons and form Ce^{3+} ions, acting as an electron trapping agent and allowing to decrease the recombination rate of the photogenerated charges in the TiO$_2$.[103] In addition, this stored oxygen can also be transferred to TiO$_2$, which increases both the rate of oxygen reduction and the efficacy of the electron–hole separation of TiO_2NPs (see schema in Fig. 3).[104]

3.4. Stability studies of the CeO_2/TiO_2 and Au/TiO_2 photocatalysts

The stability and reusability of newly developed photocatalysts is a key aspect to take into account for practical applications. In our experiments, the stability of the employed CeO_2/TiO_2 and Au/TiO_2 photocatalysts has been evaluated under sunlight for five consecutive cycles at the highest concentration of CIP/SMX used in the antibiotic degradation experiments. For each cycle, freshly prepared antibiotic solutions were used and CeO_2/TiO_2 or Au/TiO_2 were collected by centrifugation and drying the resulting pellet. Fig. 7 shows that the efficiency of CIP/SMX degradation remain stable for both photocatalysts during the first three cycles, but is reduced by *c.a.* 20% at the fifth cycle. This decrease in the degradation efficiency could be attributed to the consecutive drying and resuspension processes that may agglomerate the NPs resulting in a decrease in the available surface area for the catalytic reaction, since no leaching of metal in the supernatants after the washing cycle has been detected by ICP-MS.

4. Conclusions

Antibiotic residues in wastewaters are of particular concern due to their impact on marine and fluvial ecosystems and the development of antibiotic resistance. Different approaches have been proposed and used to remove antibiotics from water sources such as electrochemical methods, ozonation, reverse osmosis, membrane filtration, biological treatments and advanced oxidation. Among them, photocatalytic degradation using TiO_2-based nanomaterials has been widely explored in the last decades due to its high photocatalytic activity under UV light among other advantages such as its stability in a large range pH and its low-cost. To expand the TiO_2 photocatalytic activity under sun light, a wide variety of photocatalysts based on doping TiO_2 with metal ions or coupling it with light-active nanomaterials have been proposed, all with excellent results. In a typical study focusing on the photocatalytic degradation of pollutants using such nanomaterials, a photocatalyst is characterized and subsequently different parameters are modified to evaluate its activity. Herein, we aimed to evaluate and compare the photocatalytic degradation of CIP and SMX employing two different types of TiO_2 hybrid nanomaterials, semiconductor CeO_2/TiO_2 and metal Au/TiO_2, as representatives from two main families of novel photocatalysts proposed in previous scientific literature. Indeed, conducting a comprehensive comparison is a challenging task, as it involves numerous parameters related to co-catalyst characteristics, including size, shape, and addition ratio, among others. In this study, co-catalyst sizes ranging from 5 to 10 nanometers and a co-catalyst loading of 5% (at%) were employed. Both photocatalysts were extensively characterized by HR-TEM, XRD, UV-VIS, DLS, BET and XPS. The characterization showed that CeO_2/TiO_2 and Au/TiO_2 consisted of heterostructured nanocomposites containing both single component NPs in the hybrid structure and showing a decrease of the E_g values (bandgap) with respect to pure TiO_2, allowing photocatalytic reaction to occur under sunlight.

The results of the antibiotic degradation showed that although both CeO_2/TiO_2 and Au/TiO_2 show enhanced photocatalytic activity under sun irradiation, CeO_2/TiO_2 consistently exhibited the highest performance. These results suggest that the unique redox properties of CeO_2, as well as its characteristic electronic configuration and large oxygen storage capacity have a crucial role for the enhanced photocatalytic activity. Its particular electronic configuration allows CeO_2 to act as an electron trapping agent, enabling both to participate in oxidation reactions by itself and to decrease the recombination rate of the photogenerated charges in TiO_2. In addition, both TiO_2 and CeO_2 are materials with high redox potential (Ti^{4+}/Ti^{3+} and Ce^{4+}/Ce^{3+}) and their photocatalytic performance is boosted by their associated defects and oxygen vacancies, thus making CeO_2/TiO_2 hybrid nanomaterials promising candidates for a range of environmental and energetic applications.

Author contributions

M. Z. and E. C. conceptualized and designed the research. M. Z., S. J., J. T., and Y. Z. synthesized the photocatalysts and S. J., J. T., Y. L., X. L., and L. L. characterized them. M. Z., G. C., Z. J., and E. C. collected, processed and interpreted the data. M. Z., Z. J, and E. C. wrote the manuscript. All authors discussed the results, commented and reviewed the manuscript.

Conflicts of interest

The authors declare no competing financial interest.

Acknowledgements

The study was financially supported by the National Natural Science Foundation of China (22005221 to M. Z.), the Wuyi University (2018TP010 to E. C., 2018TP011 and 2020FKZX05 to M. Z.), and the Instituto de Salud Carlos III (PI19/00774 and BA22/00017 to G. C., co-funded by the European Regional Development Fund, European Union, "A way to make Europe").

References

1 X. Bai, W. Chen, B. Wang, T. Sun, B. Wu and Y. Wang, Photocatalytic Degradation of Some Typical Antibiotics: Recent Advances and Future Outlooks, *Int. J. Mol. Sci.*, 2022, **23**, 8130.

2 R. B. González-González, R. Parra-Saldívar, W. F. Alsanie and H. M. N. Iqbal, Nanohybrid catalysts with porous structures for environmental remediation through photocatalytic degradation of emerging pollutants, *Environ. Res.*, 2022, **214**, 113955.

3 F. Méndez-Arriaga, S. Esplugas and J. Giménez, Photocatalytic degradation of non-steroidal anti-

inflammatory drugs with TiO2 and simulated solar irradiation, *Water Res.*, 2008, **42**, 585–594.

4 Z. Wei, J. Liu and W. Shangguan, A review on photocatalysis in antibiotic wastewater: Pollutant degradation and hydrogen production, *Chin. J. Catal.*, 2020, **41**, 1440–1450.

5 A. Fujishima, T. N. Rao and D. A. Tryk, Titanium dioxide photocatalysis, *J. Photochem. Photobiol., C*, 2000, **1**, 1–21.

6 M. R. Prairie, L. R. Evans, B. M. Stange and S. L. Martinez, An investigation of titanium dioxide photocatalysis for the treatment of water contaminated with metals and organic chemicals, *Environ. Sci. Technol.*, 1993, **27**, 1776–1782.

7 Y. Liu, Z. Li, M. Green, M. Just, Y. Y. Li and X. Chen, Titanium dioxide nanomaterials for photocatalysis, *J. Phys. D: Appl. Phys.*, 2017, **50**, 193003.

8 A. Fujishima and X. Zhang, Titanium dioxide photocatalysis: present situation and future approaches, *C. R. Chim.*, 2006, **9**, 750–760.

9 M. Anpo, Y. Ichihashi, M. Takeuchi and H. Yamashita, Design of unique titanium oxide photocatalysts by an advanced metal ion-implantation method and photocatalytic reactions under visible light irradiation, *Res. Chem. Intermed.*, 1998, **24**, 143–149.

10 M. Haruta, Size- and support-dependency in the catalysis of gold, *Catal. Today*, 1997, **36**, 153–166.

11 D. A. Panayotov, A. I. Frenkel and J. R. Morris, Catalysis and Photocatalysis by Nanoscale Au/TiO2: Perspectives for Renewable Energy, *ACS Energy Lett.*, 2017, **2**, 1223–1231.

12 Y. Tian and T. Tatsuma, Mechanisms and Applications of Plasmon-Induced Charge Separation at TiO2 Films Loaded with Gold Nanoparticles, *J. Am. Chem. Soc.*, 2005, **127**, 7632–7637.

13 N. Zhang, S. Liu, X. Fu and Y.-J. Xu, Synthesis of M@TiO2 (M = Au, Pd, Pt) Core-Shell Nanoconnposites with Tunable Photoreactivity, *J. Phys. Chem. C*, 2011, **115**, 9136–9145.

14 L. Li, W. Ouyang, Z. Zheng, K. Ye, Y. Guo, Y. Qin, Z. Wu, Z. Lin, T. Wang and S. Zhang, Synergetic photocatalytic and thermocatalytic reforming of methanol for hydrogen production based on Pt@TiO2 catalyst, *Chin. J. Catal.*, 2022, **43**, 1258–1266.

15 S. Pany, B. Naik, S. Martha and K. Parida, Plasmon Induced Nano Au Particle Decorated over S,N-Modified TiO2 for Exceptional Photocatalytic Hydrogen Evolution under Visible Light, *ACS Appl. Mater. Interfaces*, 2014, **6**, 839–846.

16 K. Dong, J. He, J. Liu, F. Li, L. Yu, Y. Zhang, X. Zhou and H. Ma, Photocatalytic performance of Cu2O-loaded TiO2/rGO nanoheterojunctions obtained by UV reduction, *J. Mater. Sci.*, 2017, **52**, 6754–6766.

17 M. L. A. Kumari, L. G. Devi, G. Maia, T.-W. Chen, N. Al-Zaqri and M. A. Ali, Mechanochemical synthesis of ternary heterojunctions TiO2(A)/TiO2(R)/ZnO and TiO2(A)/TiO2(R)/SnO2 for effective charge separation in semiconductor photocatalysis: A comparative study, *Environ. Res.*, 2022, **203**, 111841.

18 J. A. Pinedo-Escobar, J. Fan, E. Moctezuma, C. Gomez-Solís, C. J. Carrillo Martinez and E. Gracia-Espino, Nanoparticulate Double-Heterojunction Photocatalysts Comprising TiO2(Anatase)/WO3/TiO2(Rutile) with Enhanced Photocatalytic Activity toward the Degradation of Methyl Orange under Near-Ultraviolet and Visible Light, *ACS Omega*, 2021, **6**, 11840–11848.

19 R. B. Rajput, S. N. Jamble and R. B. Kale, A review on TiO2/SnO2 heterostructures as a photocatalyst for the degradation of dyes and organic pollutants, *J. Environ. Manage.*, 2022, **307**, 114533.

20 N. Zhang, S. Liu and Y.-J. Xu, Recent progress on metal core@semiconductor shell nanocomposites as a promising type of photocatalyst, *Nanoscale*, 2012, **4**, 2227–2238.

21 Y. Chen, G. Mao, Y. Tang, H. Wu, G. Wang, L. Zhang and Q. Liu, Synthesis of core-shell nanostructured Cr2O3/C@TiO2 for photocatalytic hydrogen production, *Chin. J. Catal.*, 2021, **42**, 225–234.

22 Z. Bian, T. Tachikawa, P. Zhang, M. Fujitsuka and T. Majima, Au/TiO2 Superstructure-Based Plasmonic Photocatalysts Exhibiting Efficient Charge Separation and Unprecedented Activity, *J. Am. Chem. Soc.*, 2014, **136**, 458–465.

23 R. Jiang, B. Li, C. Fang and J. Wang, Metal/Semiconductor Hybrid Nanostructures for Plasmon-Enhanced Applications, *Adv. Mater.*, 2014, **26**, 5274–5309.

24 S. Pany and K. M. Parida, A facile in situ approach to fabricate N,S-TiO2/g-C3N4 nanocomposite with excellent activity for visible light induced water splitting for hydrogen evolution, *Phys. Chem. Chem. Phys.*, 2015, **17**, 8070–8077.

25 K. M. Parida, S. Pany and B. Naik, Green synthesis of fibrous hierarchical meso-macroporous N doped TiO2 nanophotocatalyst with enhanced photocatalytic H2 production, *Int. J. Hydrogen Energy*, 2013, **38**, 3545–3553.

26 A. Ayati, A. Ahmadpour, F. F. Bamoharram, B. Tanhaei, M. Mänttäri and M. Sillanpää, A review on catalytic applications of Au/TiO2 nanoparticles in the removal of water pollutant, *Chemosphere*, 2014, **107**, 163–174.

27 E. Kowalska, R. Abe and B. Ohtani, Visible light-induced photocatalytic reaction of gold-modified titanium(iv) oxide particles: action spectrum analysis, *Chem. Commun.*, 2009, 241–243, DOI: **10.1039/B815679D**.

28 M.-I. Mendoza-Diaz, J. Cure, M. D. Rouhani, K. Tan, S.-G. Patnaik, D. Pech, M. Quevedo-Lopez, T. Hungria, C. Rossi and A. Estève, On the UV–Visible Light Synergetic Mechanisms in Au/TiO2 Hybrid Model Nanostructures Achieving Photoreduction of Water, *J. Phys. Chem. C*, 2020, **124**, 25421–25430.

29 D. Widmann and R. J. Behm, Activation of molecular oxygen and the nature of the active oxygen species for CO oxidation on oxide supported Au catalysts, *Acc. Chem. Res.*, 2014, **47**, 740–749.

30 M. Chen, K. Luo, D. Kumar, W. T. Wallace, C. W. Yi, K. K. Gath and D. W. Goodman, The structure of ordered Au films on TiOx, *Surf. Sci.*, 2007, **601**, 632–637.

31 M. S. Chen and D. W. Goodman, Structure–activity relationships in supported Au catalysts, *Catal. Today*, 2006, **111**, 22–33.

32 Y. Maeda, Y. Iizuka and M. Kohyama, Generation of Oxygen Vacancies at a Au/TiO2 Perimeter Interface during CO Oxidation Detected by in Situ Electrical Conductance Measurement, *J. Am. Chem. Soc.*, 2013, **135**, 906–909.

33 Y. Feng, P. Ma, Z. Wang, Y. Shi, Z. Wang, Y. Peng, L. Jing, Y. Liu, X. Yu, X. Wang, X. Zhang, J. Deng and H. Dai, Synergistic Effect of Reactive Oxygen Species in Photothermocatalytic Removal of VOCs from Cooking Oil Fumes over Pt/CeO2/TiO2, *Environ. Sci. Technol.*, 2022, **56**, 17341–17351.

34 L. Gnanasekaran, S. Rajendran, A. K. Priya, D. Durgalakshmi, D.-V. N. Vo, L. Cornejo-Ponce, F. Gracia and M. Soto-Moscoso, Photocatalytic degradation of 2,4-dichlorophenol using bio-green assisted TiO2–CeO2 nanocomposite system, *Environ. Res.*, 2021, **195**, 110852.

35 J. Tian, Y. Sang, Z. Zhao, W. Zhou, D. Wang, X. Kang, H. Liu, J. Wang, S. Chen, H. Cai and H. Huang, Enhanced Photocatalytic Performances of CeO2/TiO2 Nanobelt Heterostructures, *Small*, 2013, **9**, 3864–3872.

36 J. Wang, F. Meng, W. Xie, C. Gao, Y. Zha, D. Liu and P. Wang, TiO2/CeO2 composite catalysts: synthesis, characterization and mechanism analysis, *Appl. Phys. A*, 2018, **124**, 1–6.

37 H. Eskandarloo, A. Badiei and M. A. Behnajady, TiO2/CeO2 Hybrid Photocatalyst with Enhanced Photocatalytic Activity: Optimization of Synthesis Variables, *Ind. Eng. Chem. Res.*, 2014, **53**, 7847–7855.

38 B. C. Steimle, J. L. Fenton and R. E. Schaak, Rational construction of a scalable heterostructured nanorod megalibrary, *Science*, 2020, **367**, 418–424.

39 D. G. J. Larsson, C. de Pedro and N. Paxeus, Effluent from drug manufactures contains extremely high levels of pharmaceuticals, *J. Hazard. Mater.*, 2007, **148**, 751–755.

40 J. Fick, H. Söderström, R. H. Lindberg, C. Phan, M. Tysklind and D. G. J. Larsson, Contamination of surface, ground, and drinking water from pharmaceutical production, *Environ. Toxicol. Chem.*, 2009, **28**, 2522–2527.

41 J. Bengtsson-Palme and D. G. J. Larsson, Concentrations of antibiotics predicted to select for resistant bacteria: proposed limits for environmental regulation, *Environ. Int.*, 2016, **86**, 140–149.

42 **https://www.amrindustryalliance.org/wp-content/uploads/2018/09/AMR_Industry_Alliance_List-of-Predicted-No-Effect-Concentrations-PNECs.pdf**, **https://www.amrindustryalliance.org/wp-content/uploads/2018/09/AMR_Industry_Alliance_List-of-Predicted-No-Effect-Concentrations-PNECs.pdf**, accessed May, 13, 2023.

43 G. Prasannamedha and P. S. Kumar, A review on contamination and removal of sulfamethoxazole from aqueous solution using cleaner techniques: present and future perspective, *J. Cleaner Prod.*, 2020, **250**, 119553.

44 J. O. Straub, Aquatic environmental risk assessment for human use of the old antibiotic sulfamethoxazole in Europe, *Environ. Toxicol. Chem.*, 2016, **35**, 767–779.

45 N. R. Jana, L. Gearheart and C. J. Murphy, Seeding Growth for Size Control of 5–40 nm Diameter Gold Nanoparticles, *Langmuir*, 2001, **17**, 6782–6786.

46 M. Zeng, Y. Shu, M. Parra-Robert, D. Desai, H. Zhou, Q. Li, Z. Rong, D. Ş. Karaman, H. Yang, J. Peng, G. Fernandez-Varo, W. Jiménez, G. Casals, V. Puntes, J. M. Rosenholm and E. Casals, Scalable synthesis of multicomponent multifunctional inorganic core@mesoporous silica shell nanocomposites, *Mater. Sci. Eng. C*, 2021, **128**, 112272.

47 A. Pottier, S. Cassaignon, C. Chanéac, F. Villain, E. Tronc and J.-P. Jolivet, Size tailoring of TiO2 anatase nanoparticles in aqueous medium and synthesis of nanocomposites. Characterization by Raman spectroscopy, *J. Mater. Chem.*, 2003, **13**, 877–882.

48 M. Manasa, P. R. Chandewar and H. Mahalingam, Photocatalytic degradation of ciprofloxacin & norfloxacin and disinfection studies under solar light using boron & cerium doped TiO2 catalysts synthesized by green EDTA-citrate method, *Catal. Today*, 2021, **375**, 522–536.

49 H. Wang, J. Li, C. Ma, Q. Guan, Z. Lu, P. Huo and Y. Yan, Melamine modified P25 with heating method and enhanced the photocatalytic activity on degradation of ciprofloxacin, *Appl. Surf. Sci.*, 2015, **329**, 17–22.

50 A. García, L. Delgado, J. A. Torà, E. Casals, E. González, V. Puntes, X. Font, J. Carrera and A. Sánchez, Effect of cerium dioxide, titanium dioxide, silver, and gold nanoparticles on the activity of microbial communities intended in wastewater treatment, *J. Hazard. Mater.*, 2012, **199–200**, 64–72.

51 E. Casals, E. Gonzalez and V. F. Puntes, Reactivity of inorganic nanoparticles in biological environments: insights into nanotoxicity mechanisms, *J. Phys. D: Appl. Phys.*, 2012, **45**, 443001.

52 E. Casals, M. Zeng, M. Parra-Robert, G. Fernández-Varo, M. Morales-Ruiz, W. Jiménez, V. Puntes and G. Casals, Cerium Oxide Nanoparticles: Advances in Biodistribution, Toxicity, and Preclinical Exploration, *Small*, 2020, **16**, 1907322.

53 D. T. Thompson, Using gold nanoparticles for catalysis, *Nano Today*, 2007, **2**, 40–43.

54 M. Parra-Robert, E. Casals, N. Massana, M. Zeng, M. Perramón, G. Fernández-Varo, M. Morales-Ruiz, V. Puntes, W. Jiménez and G. Casals, Beyond the Scavenging of Reactive Oxygen Species (ROS): Direct Effect of Cerium Oxide Nanoparticles in Reducing Fatty Acids Content in an In Vitro Model of Hepatocellular Steatosis, *Biomolecules*, 2019, **9**, 425.

55 L. S. R. Rocha, A. Z. Simões, C. Macchi, A. Somoza, G. Giulietti, M. A. Ponce and E. Longo, Synthesis and defect characterization of hybrid ceria nanostructures as a possible novel therapeutic material towards COVID-19 mitigation, *Sci. Rep.*, 2022, **12**, 3341.

56 O. Zuas and N. Hamim, Synthesis, Characterization and Properties of CeO2-doped TiO2 Composite Nanocrystals, *Mater. Sci.*, 2013, **19**, 443–447.

57 Y. Li, W. Li, F. Liu, M. Li, X. Qi, M. Xue, Y. Wang and F. Han, Construction of CeO2/TiO2 heterojunctions immobilized on activated carbon fiber and its synergetic effect between adsorption and photodegradation for toluene removal, *J. Nanopart. Res.*, 2020, **22**, 122.

58 M. Wang, J. Ioccozia, L. Sun, C. Lin and Z. Lin, Inorganic-modified semiconductor TiO2 nanotube arrays for photocatalysis, *Energy Environ. Sci.*, 2014, **7**, 2182–2202.

59 U. Balachandran and N. G. Eror, Raman spectra of titanium dioxide, *J. Solid State Chem.*, 1982, **42**, 276–282.

60 V. Swamy, A. Kuznetsov, L. S. Dubrovinsky, P. F. McMillan, V. B. Prakapenka, G. Shen and B. C. Muddle, Size-Dependent Pressure-Induced Amorphization in Nanoscale ${\mathrm{TiO}}_{2, *Phys. Rev. Lett.*, 2006, **96**, 135702.

61 S. Pany and K. M. Parida, Sulfate-Anchored Hierarchical Meso–Macroporous N-doped TiO2: A Novel Photocatalyst for Visible Light H2 Evolution, *ACS Sustain. Chem. Eng.*, 2014, **2**, 1429–1438.

62 H. Abdullah, M. R. Khan, M. Pudukudy, Z. Yaakob and N. A. Ismail, CeO2-TiO2 as a visible light active catalyst for the photoreduction of CO2 to methanol, *J. Rare Earths*, 2015, **33**, 1155–1161.

63 N. Aman, P. K. Satapathy, T. Mishra, M. Mahato and N. N. Das, Synthesis and photocatalytic activity of mesoporous cerium doped TiO2 as visible light sensitive photocatalyst, *Mater. Res. Bull.*, 2012, **47**, 179–183.

64 Z. Fan, F. Meng, J. Gong, H. Li, Y. Hu and D. Liu, Enhanced photocatalytic activity of hierarchical flower-like CeO2/TiO2 heterostructures, *Mater. Lett.*, 2016, **175**, 36–39.

65 G. Vieira, H. José, M. Peterson, V. Baldissarelli, P. Alvarez and R. Moreira, CeO 2/TiO 2 nanostructures enhance adsorption and photocatalytic degradation of organic compounds in aqueous suspension, *J. Photochem. Photobiol., A*, 2017, **353**, 325–336.

66 H. Li, G. Wang, F. Zhang, Y. Cai, Y. Wang and I. Djerdj, Surfactant-assisted synthesis of CeO2 nanoparticles and their application in wastewater treatment, *RSC Adv.*, 2012, **2**, 12413–12423.

67 J. B. Coulter and D. P. Birnie III, Assessing Tauc Plot Slope Quantification: ZnO Thin Films as a Model System, *Phys. Status Solidi B*, 2018, **255**, 1700393.

68 J. Tauc, R. Grigorovici and A. Vancu, Optical Properties and Electronic Structure of Amorphous Germanium, *Phys. Status Solidi B*, 1966, **15**, 627–637.

69 E. A. Davis and N. F. Mott, Conduction in non-crystalline systems V. Conductivity, optical absorption and photoconductivity in amorphous semiconductors, *Philos. Mag. A*, 1970, **22**, 0903–0922.

70 J. Klein, L. Kampermann, B. Mockenhaupt, M. Behrens, J. Strunk and G. Bacher, Limitations of the Tauc Plot Method, *Adv. Funct. Mater.*, 2023, 2304523.

71 S. Ameen, M. Shaheer Akhtar, H.-K. Seo and H.-S. Shin, Solution-processed CeO2/TiO2 nanocomposite as potent visible light photocatalyst for the degradation of bromophenol dye, *Chem. Eng. J.*, 2014, **247**, 193–198.

72 H. Sun, Q. He, P. She, S. Zeng, K. Xu, J. Li, S. Liang and Z. Liu, One-pot synthesis of Au@TiO2 yolk-shell nanoparticles with enhanced photocatalytic activity under visible light, *J. Colloid Interface Sci.*, 2017, **505**, 884–891.

73 R. Jaiswal, N. Patel, A. Dashora, R. Fernandes, M. Yadav, R. Edla, R. S. Varma, D. C. Kothari, B. L. Ahuja and A. Miotello, Efficient Co-B-codoped TiO2 photocatalyst for degradation of organic water pollutant under visible light, *Appl. Catal., B*, 2016, **183**, 242–253.

74 R. Shetty, V. B. Chavan, P. S. Kulkarni, B. D. Kulkarni and S. P. Kamble, Photocatalytic Degradation of Pharmaceuticals Pollutants Using N-Doped TiO2 Photocatalyst: Identification of CFX Degradation Intermediates, *Indian Chem. Eng.*, 2017, **59**, 177–199.

75 M. N. Abellán, B. Bayarri, J. Giménez and J. Costa, Photocatalytic Degradation of Sulfamethoxazole in Aqueous Suspension of TiO2, *Appl. Catal., B*, 2007, **74**, 233–241.

76 E. Borowska, J. F. Gomes, R. C. Martins, R. M. Quinta-Ferreira, H. Horn and M. Gmurek, Solar Photocatalytic Degradation of Sulfamethoxazole by TiO2 Modified with Noble Metals, *Catalysts*, 2019, **9**, 500.

77 J. C. Durán-Álvarez, E. Avella, R. M. Ramírez-Zamora and R. Zanella, Photocatalytic degradation of ciprofloxacin using mono- (Au, Ag and Cu) and bi- (Au–Ag and Au–Cu) metallic nanoparticles supported on TiO2 under UV-C and simulated sunlight, *Catal. Today*, 2016, **266**, 175–187.

78 X. Zheng, S. Xu, Y. Wang, X. Sun, Y. Gao and B. Gao, Enhanced degradation of ciprofloxacin by graphitized mesoporous carbon (GMC)-TiO2 nanocomposite: strong synergy of adsorption-photocatalysis and antibiotics degradation mechanism, *J. Colloid Interface Sci.*, 2018, **527**, 202–213.

79 H. Gong and W. Chu, Determination and toxicity evaluation of the generated products in sulfamethoxazole degradation by UV/CoFe2O4/TiO2, *J. Hazard. Mater.*, 2016, **314**, 197–203.

80 S. P. Pattnaik, A. Behera, S. Martha, R. Acharya and K. Parida, Facile synthesis of exfoliated graphitic carbon nitride for photocatalytic degradation of ciprofloxacin under solar irradiation, *J. Mater. Sci.*, 2019, **54**, 5726–5742.

81 X. Yu, J. Zhang, J. Zhang, J. Niu, J. Zhao, Y. Wei and B. Yao, Photocatalytic degradation of ciprofloxacin using Zn-doped Cu2O particles: analysis of degradation pathways and intermediates, *Chem. Eng. J.*, 2019, **374**, 316–327.

82 T. A. Gad-Allah, M. E. Ali and M. I. Badawy, Photocatalytic oxidation of ciprofloxacin under simulated sunlight, *J. Hazard. Mater.*, 2011, **186**, 751–755.

83 Y. Yan, X. Liu, W. Fan, P. Lv and W. Shi, InVO4 microspheres: preparation, characterization and visible-light-driven photocatalytic activities, *Chem. Eng. J.*, 2012, **200–202**, 310–316.

84 T. An, H. Yang, G. Li, W. Song, W. J. Cooper and X. Nie, Kinetics and mechanism of advanced oxidation processes (AOPs) in degradation of ciprofloxacin in water, *Appl. Catal., B*, 2010, **94**, 288–294.

85 M. Malakootian, A. Nasiri and M. Amiri Gharaghani, Photocatalytic degradation of ciprofloxacin antibiotic by TiO2 nanoparticles immobilized on a glass plate, *Chem. Eng. Commun.*, 2020, **207**, 56–72.

86 A. Salma, S. Thoröe-Boveleth, T. C. Schmidt and J. Tuerk, Dependence of transformation product formation on pH during photolytic and photocatalytic degradation of ciprofloxacin, *J. Hazard. Mater.*, 2016, **313**, 49–59.

87 F. Zheng, P. M. Martins, J. M. Queirós, C. J. Tavares, J. L. Vilas-Vilela, S. Lanceros-Méndez and J. Reguera, Size Effect in Hybrid TiO2:Au Nanostars for Photocatalytic Water Remediation Applications, *Int. J. Mol. Sci.*, 2022, **23**, 13741.

88 S. Krishnan and A. Shriwastav, Chlorophyll sensitized and salicylic acid functionalized TiO2 nanoparticles as a stable and efficient catalyst for the photocatalytic degradation of ciprofloxacin with visible light, *Environ. Res.*, 2023, **216**, 114568.

89 L. Li, J. Liu, J. Zeng, J. Li, Y. Liu, X. Sun, L. Xu and L. Li, Complete Degradation and Detoxification of Ciprofloxacin by a Micro-/Nanostructured Biogenic Mn Oxide Composite from a Highly Active Mn(2+)-Oxidizing Pseudomonas Strain, *Nanomaterials*, 2021, **11**, 1660.

90 W. Shi, Y. Yan and X. Yan, Microwave-assisted synthesis of nano-scale BiVO4 photocatalysts and their excellent visible-light-driven photocatalytic activity for the degradation of ciprofloxacin, *Chem. Eng. J.*, 2013, **215–216**, 740–746.

91 P. Huo, M. Zhou, Y. Tang, X. Liu, C. Ma, L. Yu and Y. Yan, Incorporation of N–ZnO/CdS/Graphene oxide composite photocatalyst for enhanced photocatalytic activity under visible light, *J. Alloys Compd.*, 2016, **670**, 198–209.

92 J. Yao, Z. Gao, Q. Meng, G. He and H. Chen, One-step synthesis of reduced graphene oxide based ceric dioxide modified with cadmium sulfide (CeO2/CdS/RGO) heterojunction with enhanced sunlight-driven photocatalytic activity, *J. Colloid Interface Sci.*, 2021, **594**, 621–634.

93 M. Yan, F. Zhu, W. Gu, L. Sun, W. Shi and Y. Hua, Construction of nitrogen-doped graphene quantum dots-BiVO4/g-C3N4 Z-scheme photocatalyst and enhanced photocatalytic degradation of antibiotics under visible light, *RSC Adv.*, 2016, **6**, 61162–61174.

94 L. Wolski, K. Grzelak, M. Muńko, M. Frankowski, T. Grzyb and G. Nowaczyk, Insight into photocatalytic degradation of ciprofloxacin over CeO2/ZnO nanocomposites: unravelling the synergy between the metal oxides and analysis of reaction pathways, *Appl. Surf. Sci.*, 2021, **563**, 150338.

95 Y. Yan, S. Sun, Y. Song, X. Yan, W. Guan, X. Liu and W. Shi, Microwave-assisted in situ synthesis of reduced graphene oxide-BiVO4 composite photocatalysts and their enhanced photocatalytic performance for the degradation of ciprofloxacin, *J. Hazard. Mater.*, 2013, **250–251**, 106–114.

96 J.-D. Cafun, K. O. Kvashnina, E. Casals, V. F. Puntes and P. Glatzel, Absence of Ce3+ Sites in Chemically Active Colloidal Ceria Nanoparticles, *ACS Nano*, 2013, **7**, 10726–10732.

97 C. T. Campbell and C. H. F. Peden, Oxygen Vacancies and Catalysis on Ceria Surfaces, *Science*, 2005, **309**, 713–714.

98 F. Esch, S. Fabris, L. Zhou, T. Montini, C. Africh, P. Fornasiero, G. Comelli and R. Rosei, Electron Localization Determines Defect Formation on Ceria Substrates, *Science*, 2005, **309**, 752–755.

99 M. Nolan, S. C. Parker and G. W. Watson, The electronic structure of oxygen vacancy defects at the low index surfaces of ceria, *Surf. Sci.*, 2005, **595**, 223–232.

100 E. G. Heckert, S. Seal and W. T. Self, Fenton-Like Reaction Catalyzed by the Rare Earth Inner Transition Metal Cerium, *Environ. Sci. Technol.*, 2008, **42**, 5014–5019.

101 J. F. Jerratsch, X. Shao, N. Nilius, H. J. Freund, C. Popa, M. V. Ganduglia-Pirovano, A. M. Burow and J. Sauer, Electron localization in defective ceria films: a study with scanning-tunneling microscopy and density-functional theory, *Phys. Rev. Lett.*, 2011, **106**, 246801.

102 H. C. Yao and Y. F. Y. Yao, Ceria in automotive exhaust catalysts: I. Oxygen storage, *J. Catal.*, 1984, **86**, 254–265.

103 B. Jiang, S. Zhang, X. Guo, B. Jin and Y. Tian, Preparation and photocatalytic activity of CeO2/TiO2 interface composite film, *Appl. Surf. Sci.*, 2009, **255**, 5975–5978.

104 V. Kumari, A. Sharma, N. Kumar, M. Sillanpää, P. R. Makgwane, M. Ahmaruzzaman, A. Hosseini-Bandegharaei, M. Rani and P. Chinnamuthu, TiO2-CeO2 assisted heterostructures for photocatalytic mitigation of environmental pollutants: a comprehensive study on band gap engineering and mechanistic aspects, *Inorg. Chem. Commun.*, 2023, **151**, 110564.